# A Flexible, Low-Power Platform for UAV-Based Data Collection From Remote Sensors

**TOMMASO POLONELLI**[1], **(Student Member, IEEE), YUAN QIN**[2], **(Student Member, IEEE),**
**ERIC M. YEATMAN**[2], **(Fellow, IEEE), LUCA BENINI**[1], **(Fellow, IEEE),**
**AND DAVID BOYLE**[2], **(Member, IEEE)**
[1]DEI, Università degli studi di Bologna, 40127 Bologna, Italy
[2]Dyson, Imperial College London, London SW7 2AZ, U.K.

Corresponding author: Tommaso Polonelli (tommaso.polonelli2@unibo.it)

**ABSTRACT** This article presents the design and characterisation of a new low-power hardware platform to integrate unmanned aerial vehicle and wireless sensor technologies. In combination, these technologies can overcome data collection and maintenance problems of *in situ* monitoring in remote and extreme environments. Precision localisation in support of maximum efficiency mid-range inductive power transfer when recharging devices and increased throughput between drone and device are needed for data intensive monitoring applications, and to balance proximity time for devices powered by supercapacitors that recharge in seconds. The platform described in this article incorporates ultra-wideband technology to achieve high-performance ranging and high data throughput. It enables the development of a new localisation system that is experimentally shown to improve accuracy by around two orders of magnitude to 10 cm with respect to GNSS and achieves almost 6 Mbps throughput in both lab and field conditions. These results are supported by extensive modelling and analysis. The platform is designed for application flexibility, and therefore includes a wide range of sensors and expansion possibilities, with source code for two applications made immediately available as part of a open source project to support research and development in this new area.

**INDEX TERMS** Autonomous vehicles, unmanned autonomous vehicles, unmanned aerial vehicles, radio navigation, wireless power transmission, wireless sensor networks, ultra wideband communication, printed circuits, open source hardware, open source software.

## I. INTRODUCTION

Remote monitoring under challenging conditions continues to present problems to prospective practitioners. Lack of infrastructure communications networks over which to transmit data to internet-connected servers and difficulty with the maintenance of finite energy devices are chief among these problems. Emerging 5G networks are likely to continue to suffer from coverage problems in remote areas or in sparsely populated regions where infrastructure investment is economically unattractive, and therefore offer no silver bullet for ubiquitous connectivity. Similarly, energy harvesting technologies and advances in low power wireless sensing systems have yet to deliver on the promise of energy neutral long-term operation at large scale [1].

Recent advances integrating inexpensive unmanned aerial vehicle (UAV), or *drone*, platforms with *in situ* wireless

The associate editor coordinating the review of this manuscript and approving it for publication was Halil Ersin Soken.

sensors, where the former is responsible for both data collection and energy buffer replenishment of the latter, can pave the way to delivering long-lasting monitoring systems in remote and extreme environments [2]. Under such circumstances, it is assumed that drones may be deployed from a station that has an internet connection and the ability to recharge the drone itself, to service a sensing field that may span many square kilometres. Remote sensing devices may be tasked with collecting a variety of heterogeneous time series data sets to be retrieved by a drone at periodic intervals, while at the same time recharging the device's battery or other energy store. This poses several relatively novel challenges, including the design of appropriate communication and localisation mechanisms.

In addition to reliable throughput and low power operation [3], [4], communications protocols designed for these purposes must also contribute to precise localisation in support of wireless charging, where sub-metre accuracy is required for inductive wireless power transfer. Although

transceivers implementing the aforementioned wireless technologies offer received signal strength indicators (RSSI) that can be used for ranging, it is well understood that this measure is insufficiently accurate or granular for the purposes of sub-metre localisation [5].

Ultra-wide band (UWB) technology (IEEE 802.15.4-2011), on the other hand, is attractive in this regard, as it is both energy efficient in terms of per bit consumption and offers high-accuracy ranging between two points. In fact, the energy cost per bit is measured in the nJ range and ranging accuracy at the centimetre level has been demonstrated [6]. Surprisingly, there are no *off-the-shelf* wireless sensor devices that incorporate a UWB wireless interface. Therefore, motivated to continue work on the development of communications and localisation technologies to enable UAV-sensor data collection and power transfer, it was necessary to design and build a new hardware platform. The objective was to leverage the advantages of existing communication standards with low network maintenance energy costs in combination with emerging UWB technology, offering further advantages in per bit energy and ranging performance.

This article describes the design and characterisation of the new hardware platform, which focuses on application-level flexibility from the outset. The platform thus facilitates a variety of sensing tasks and is mindful of the many different sampling frequencies that may be required. Soil moisture monitoring or corrosion detection applications, for example, may require only a few readings per day, whereas structural health monitoring or other event detecting applications may require in excess of hundreds of Hz. The platform has therefore been designed to provide the capabilities of collecting, processing, storing, and transmitting sampled data from a variety of sensors. Data throughput must be sufficient to deliver the data to the UAV within the charging period. As Global Navigation Satellite Systems, such as GPS, provide only meter-level accuracy, for the proper alignment of two inductive power transfer coils, centimetre level navigation accuracy is required.

The contributions of this article can be summarised as follows:

- Design and characterisation of a new hardware platform to support UAV-based remote monitoring operations, including precision localisation and wireless power transfer;
- A UWB ranging protocol capable of streaming time-of-flight and induced coil voltage information in real-time;
- Detailed experimentally obtained energy and ranging performance results;
- A *first-of-its-kind* hardware and software platform provided open source[1] to the community that is flexible to meet the needs of a variety of application scenarios.

The rest of the paper is organized as follows. Related works are discussed in Section II. The system architecture

[1] https://github.com/tommasopolonelli/SynthSense-WSN-UAV

is described in Sections III, III-A, and III-B, while in Section III-C a novel multi-stage navigation support approach is explained. In Section IV, the hardware platform equipped with both UWB and WPT is detailed. Section V describes the hardware performance under two-way ranging experiments. Section V-C describes the ranging and data transfer protocol. A detailed analytical model of each component is evaluated in Section VI against measurements collected experimentally. Finally, Section VIII concludes the paper.

## II. RELATED WORKS

In general, UAVs use information from sensors to perform actions including adjusting route and speed, obstacle avoidance [7], [8], and object tracking [9]. However, precision landing is still an unsolved problem in the UAV research field [4]. In [10], the authors discuss design considerations and present a system that allows a drone to fly to remote locations, and to wireless charge difficult to access sensors. Since the GPS does not provide sufficient accuracy [11], they develop a relative localisation algorithm based on sensing the magnetic field of the power transfer system with an average error of 15 cm and a maximum power transfer of 4.2 W. In this work, we combine elements of the relative localisation system based on sensing the magnetic field presented in [10] with results from [12], [13], which describe a high efficiency (70%) inductive power transfer system (IPT), to create a system capable of 150 W instantaneous WPT (Wireless Power Transfer) with real-time feedback for the UAV's precision landing algorithm. Our work focuses on charging static terrestrial devices, although charging of drones has been considered in the literature ranging from similar IPT techniques to harvesting from power lines [14].

Using a combined GPS and wireless power transfer localisation system, precision landing can be performed. However, in a real deployment, and due to the limited operational range of the WPT, the UAV still has unpredictable path selection in the 10 m to 50 cm region, where GPS is unreliable and the WPT subsystem cannot couple. For example, in [15], the authors describe a WPT localisation system that uses a lookup table of induced voltages and is accurate in the range from 0.2 m to 1.5 m. This is a promising approach building upon prior work in resonant power transfer to ground sensors [16], but is limited by the amount of power shown to be transferred (i.e. 6.1 W at peak efficiency) and does not consider high speed, low power data transfer between the UAV and sensor node.

In the literature, there are many examples of autonomous drones and swarms of drones employing Ultra Wide Band (UWB) technology [6], [17]–[20], that has been proven a reliable technology for precision ranging in moving object environments. Researchers have recognised this potential, and proposed bespoke UWB antennas for UAV applications [21]. Indeed, UWB enables indoor and outdoor ranging within 100 m range and features a high interference immunity, as well as low Doppler-effect sensitivity due to UWB physical properties and coded modulation. In [17] a

GNSS-denied navigation system for UAV is presented; while in [18], Chiaberge uses the UWB for robotic applications. Lastly, in [20] and [22], the authors investigate the fundamental limits of UWB ranging accuracy in high-definition localisation systems. All the aforementioned works make use of the Decawave DW1000 UWB transceiver [23], which can achieve 5 cm precision in a working range of 100 m. This is an ideal candidate solution to cover the range between 10 m to 50 cm. Moreover, the DW1000 enables high-speed data transfer [24], as tested in [25], reaching up to 6.8 Mbps.

The purpose of this article is threefold, enabling WPT for hard to access sensor nodes with precision landing support for UAVs and fast bi-directional data transfer. Qin *et al.* propose the first concept of a three stage localisation mechanism in [4]. The paper provides a solid basis to develop maximally efficient wireless power transfer mechanisms to recharge static sensors using a combination of GPS, Bluetooth Low Energy and WPT to find the optimal position from which to transmit power. Due to the adopted signal strength indicator (RSSI) method for the position estimation, they suffer from a high packet loss, in reality relying only on the GNSS and WPT [4]. The system proposed in this article leverages the considerations in [4] as a starting point for the proposed low-power sensor platform, using the UWB position estimation instead of RSSI to enable precision localisation.

There are numerous detailed surveys and works concerning UAVs [26], [27] and their application in industrial and civil scenarios to be found in the literature, including making use of emerging cellular technologies like NB-IoT [28] or using drones to extend cellular coverage and aggregate sensor data [29]. Complementary systems, like autopilot for unmanned aerial vehicles [30] and navigation systems that combine visual odometry with inertial measurements from IMUs [31]–[33], are also documented. To the best of our knowledge, however, there is no hardware and software design support for energy efficient wireless sensor devices that can be readily integrated with UAV platforms that also deliver precision localisation. This work is proposed to deliver precise point-to-point localisation, high speed data transfer and wireless power transfer, particularly suited to applications in remote and extreme environments.

## III. THE SUPPORTED FRAMEWORK
This section briefly presents the principle of operation of the three-stage system for wirelessly charging sensor nodes. The conceptual setup of the UAV, often referred as a *drone*, and the overall system settings are described, in Fig. 1. Subsequently, the UAV on-board control framework and concept of multi-stage navigation are introduced.

### A. SYSTEM OVERVIEW
The UAV is responsible for autonomously flying between its originating point and designated wireless sensor devices. Upon arriving at the destination, the drone charges the sensor node's batteries, landing or hovering as close as possible to the inductive power transfer (IPT) receive coil, where
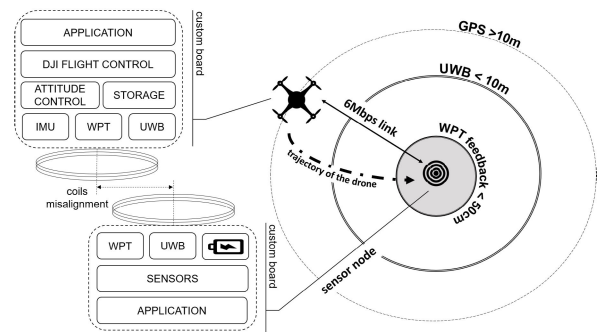


**FIGURE 1.** System overview; incorporates three stage navigation.

charging efficiency is monitored via a high-speed wireless link between the UAV and the node. Meanwhile, the information stored in its internal memory (e.g time series sensor data) is also uploaded to the UAV. Finally, the UAV moves to the next targeted node and repeats the process. Although the design of an optimal flying path or route optimisation are relevant to this work, these are beyond the scope of this article and hence not further discussed [11], [34].

The WPT module of the UAV delivers energy via the power circuit and the transmitting coil, directly connected to the main battery. A specific module from DJI [35] manages the UAV attitude during all flight manoeuvres, including take-off, hovering, cruise, and landing. The application layer includes the on-board computer, the sensor data storage, and flight sensors. On the sensor node side, the UWB transceiver on the sensor node reports the inductive voltage generated at the receiving coil. The UAV then makes decisions to fly to the location where the inductive voltage becomes the maximum, following a 2D gradient descendent algorithm, as presented in Fig. 1. The inductive voltage based localisation is discussed in section IV-A.

### B. THE UAV CONTROL FRAMEWORK
The framework provides interactions between drone hardware and software. The UAV combines its telemetry information with UWB data so that the speed and GPS coordinates are updated in real-time, as well as the scalar distance between the drone and the sensor node. In parallel, the UWB chip streams the received inductive voltage, which helps the UAV with the inductive localisation.

The software workflow of the control layer is structured as follows. The UAV algorithm receives the relative three-dimensional position between the transmitting and the receiving coils, which indicates how much further the UAV needs to fly, while then it takes the on-board telemetry, which includes a gyroscope, one magnetometer and, a 3-axes accelerometer, as well as UWB distance scalar, and ultrasonic sensor inputs used to determine the relative position.

### C. MULTI-STAGE NAVIGATION
The sensors to be used in the UAV approach control are listed in Table 1. Using standalone GPS navigation does not

**TABLE 1.** Sensors for On-board control framework.

| Sensors | Working Range (m) | Error (m) | Output |
|---|---|---|---|
| GPS | $0 - \infty$ | 10 | 3D Coordinates |
| UWB | $0.2 - 100$ | 0.03 | Distance Scalar |
| Coil voltage | $0 - 0.5^*$ | 0.01 | Voltage Reading |
| Ultrasonic | $0.2 - 7.5$ | 0.01 | Distance Scalar |

\* The max working range is determined by the height of the drone at the landing path.

provide enough accuracy for the inductive power transfer specifications, which require a landing precision with a maximum lateral misalignment of tens of cm to keep the charging efficiency at ~70% [12]. The drone uses several sensors to improve flight control accuracy. The UWB distance sensor has a wide range of operation and good accuracy, about 5 cm. It works from 20 cm to around 100 m, where the upper bound depends on the transmitting power and the antenna radiation patterns. The inductive voltage changes significantly when the relative position between the transmitting and the receiving coil shifts towards or away from perfect alignment and close contact. The maximum working distance of the voltage sensor is determined by the geometry of both the transmitting and receiving coil. In this article, it is about 50 cm, see Table 1 and Eq. 1. According to the accuracy and the working range of the listed sensors, three stages of navigation are thus proposed. The first stage of navigation needs only the GPS system, which guides the UAV from anywhere to a circular range of 10 ($d'$) meters from the desired location, see Fig. 1. The UAV has *a priori* knowledge of the GPS coordinates of the nodes, i.e. stored in internal memory. These destination points are saved as latitude and longitude coordinates, with an accuracy assumed to be within 10 m. Since the UWB communication range reaches up to 100 m, the UAV control framework supports sensor shifts or movements greater than 10 m. This may be a valuable feature in real applications, where animals or other extraneous processes may move the sensor node from its original position. During the first stage, the altitude could be a fixed safety level, but, at the end of the first stage, a maximum relative elevation from the sensor node of a couple of meters should be kept, an empirical value useful to optimise the distance measurement. The second stage of the navigation (Fig. 1) starts from 10 metres ($d'$) away from the sensor node's UWB antenna, receiving only the point-to-point scalar distance. The ranging process allows the drone to estimate the distance $d_{ATWR} = \|d - s\|$, with $d$ and $s$ being the drone and the sensor location, respectively. To calculate a planar distance, a precise altitude value is required from the ultrasonic sensor. Lastly, the third stage begins from about 50 centimetres to the targeted location. This is the last stage of the navigation, which aims to perfectly align two inductive coils for the IPT.

## IV. HARDWARE
### A. TECHNICAL SPECIFICATION
The hardware platform comprises two PCBs, the sensor board and power electronics board (PEB), respectively; shown

in Fig. 2. The two boards are connected via a 16-pin JST connector, shown schematically in Fig. 3 and pictured in Fig. 2. The power electronics board deals with tasks related to the power supply, including generating reliable and stable 3.3 V and 5 V DC voltage from two Panasonic 18650 batteries, managing fast-charging and the wireless power transfer system that supports up to 150 W.
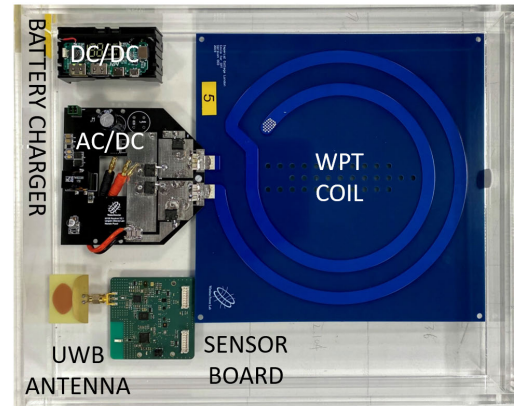


**FIGURE 2.** Complete receiver side hardware. The coil used for wireless power transfer (blue), sensor board (green, bottom left) and battery management circuits (DC/DC and AC/DC; black boxes) are shown. The UWB antenna is directly connected to the sensor board.

The PEB that manages the wireless power delivered by the quadcopter, including operating principle and performance characterisation, is discussed in [12], [13]. Under our scenario, the WPT system consists of two coils; a transmitting coil connected to a drone and a receiving coil incorporated into the PEB. A magnetic field, coupled with the receiver coil, is generated by driving the transmitting coil with an alternating current, which induces a voltage across the PEB. The transmitting and receiving coils have different sizes and are separated by variable distance and different degrees of misalignment, thus varying the coupling coefficient as the drone is approaching and landing by the sensor node. The coefficient $k$ describes the coupling between the two coils:

$$k = \frac{M}{\sqrt{L_p L_s}}. \tag{1}$$

where $L_s$ and $L_p$ are respectively self-inductances of the receiving and transmitting coils; the mutual inductance is defined as $M$, which decreases when increasing the distance between two coils, i.e., the distance between the drone and sensor node. The accurate expression of mutual inductance and its numerical calculation method is describe in [36]. A higher value of $k$ (up to a maximum of 1) indicates that a large portion of the magnetic field generated by the drone's coil is coupled into the sensor node's coil, hence monitoring the receiver inductive voltage is helpful to estimate the distance between the devices. For this reason, the sensor board has a dedicated analog channel connected to the receiver coil, as shown in Fig. 3. Hence, to estimate the coil-to-coil distance, the UAV makes use of a look-up table that
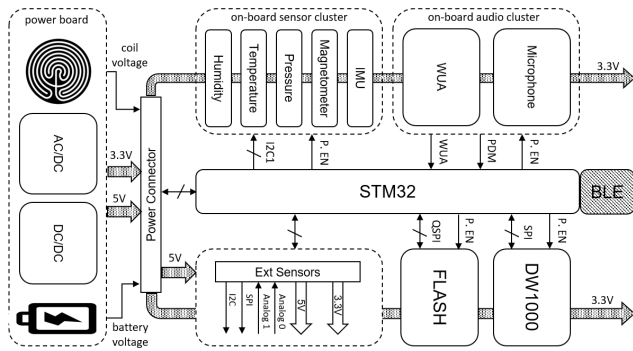
**FIGURE 3.** Sensor board schematic. The power connector splits the power electronics and sensor boards.

correlates distance with the measured voltage similar to [15]; shown in Fig. 8. This method needs an initial calibration but enables the use of a real-time routine that provides reliable distance estimation. As the details of the PEB are available in [12] and [13], the remainder of this section focuses on the digital and wireless aspects of the sensor node that facilitates precise localisation to ensure high-efficiency coupling, high data throughput and energy efficient operation.

### B. SENSOR NODE

The proposed sensor board features a multi-protocol radio front-end and many complementary sensors, internal and external, to support a variety of sensor-fusion and UAV applications. The PCB dimension is $70 \times 70$ mm combined with the external UWB antenna of $30 \times 40$ mm. The sensor node is specifically designed to be a general purpose and versatile device. Moreover, it needs only low cost off-the-shelf components, a prerequisite for open source projects. It is optimised to be used in combination with drones, but can be easily deployed in other application scenarios, such as smart agriculture and Industrial Internet of Things (IIoT). The hardware's schematic and the firmware (with two different demos), as well as all the data collected in our in-field experiment are published as general public licence on GitHub [37]. To support the aforementioned three stage landing procedure and the WPT, the hardware includes an UWB transceiver and the coil voltage measurement, but it can be utilised as a reference to develop and test new localisation methods or to improve the overall system performance.

An integrated STM32WB55RGV (STM32 hereafter) from ST Microelectronics manages all the stacks and sensors. This MCU has the advantages of low power consumption, as well as excellent peripherals support. The ARM Cortex-M4 is used for the main processing tasks, while the ARM Cortex-M0 is the radio communication protocols engine. To decrease the power consumption in sleep and deep-sleep states, the circuit implements four voltage supply domains. The STM32 enables or disables each domain depending on application requirements and operating modes. The board integrates temperature (TMP117), humidity (HDC2080) and

digital pressure (BMP280) sensors. To expand application support, the board integrates two high-frequency sensors, a 3D inertial IC (LSM6DSOX) and a digital magnetometer (IIS2MDC) from ST Microelectronics. In addition to the on-board ICs, the device can incorporate external analogue and digital sensors through a 16-pin connector (*Ext Sensors* in Fig. 3).

In addition to the aforementioned environmental sensors, the sensor board enables audio recording. A digital microphone (IMP34DT05) from ST Microelectronics combined with an ultra-low-power wake-up audio (WUA) sub-circuit (capable of waking up the MCU on triggering events when the environment sound is above a predetermined threshold) are included. Exploiting the wake-up method, the MCU can store only relevant information, and remain in sleep mode during periods of 'inactivity'. The MP23ABS1 is a compact, low-power analog microphone built with a capacitive sensing element, and it is the main WUA component together with a micro-watt comparator (LTC6259). The WUA requires only 160 $\mu$A at 3.3 V, drastically reducing the average power consumption of the audio recording sub-circuit and the size of non-volatile memory required (more details in Table 3).

The MCU's internal flash is not sufficient for data-intensive continuous sampling storage. A 256 MB external flash (MT25QL256ABA) is used to store audio data at a 16 ksps.

A detailed power consumption description and analysis are presented in the following sections.

### C. DECAWAVE DW1000

The DW1000 [23] is a low power UWB radio transceiver compliant with IEEE 802.15.4-2011. The DW1000 supports real-time location estimation using both two-way ranging and time difference of arrival schemes. The radio interface is fully configurable and supports six bands between 3.5 GHz and 6.5 GHz with two configurable data rates: 100 kbps and 6.8 Mbps. The serial interface works on top of a 20 MHz SPI bus, which in parallel with a single interrupt line, manages the bi-directional communication with the STM32. The chipping rate given by the IEEE 802.15.4-2011 standard [24] is 499.2 MHz, equal to the bandwidth (BW). Hence, the DW1000 system clocks are referenced to this frequency, providing a 63.8976 GHz sampling clock with a period of 15.65 ps. The DW1000 physical layer device is a carrier-based impulse radio that can only generate $+1$ or $-1$ UWB pulses with a bandwidth of 499.2 MHz at the selected carrier frequency. The preamble is composed of a ternary alphabet spread at the nominal pulse repetition frequency (PRF), making a unique code with perfect periodic auto-correlation and low cross-correlation properties. The signal modulation settings related to each mode of operation are listed in Table 2. The preamble length $Preamble_p$ and its code ($Code_p$) are defined by the IEEE 802.15.4-2011 standard, while the $CH_p$ frequency can be selected to avoid inter-channel interference. The DW1000 has nine different power operation states: OFF, WAKEUP, INIT, IDLE, SLEEP,

**TABLE 2.** STM32 and DW1000 details.

| Symbol | Description | Value |
|---|---|---|
| $V_s$ | sensor board voltage supply | 3.3 V |
| $I_{active}^{MCU}$ | STM32 run current | 7.59 mA |
| $I_{idle}^{MCU}$ | STM32 idle current | 4.15 mA |
| $I_{stop}^{MCU}$ | STM32 stop current | 2.45 $\mu$A |
| $I_t^{MCU}$ | STM32 transition current $stop \rightarrow run$ | 7.59 mA |
| $t_t^{MCU}$ | STM32 transition time $stop \rightarrow run$ | 5.71 $\mu$s |
| $I_{BLE}^{MCU}$ | STM32 BLE current advertising | 30 $\mu$A |
| | (Tx = 0 dBm; Period 1 s; 31 B) | |
| $Mode(p)$ | DW1000 Op. Mode | $p \in \mathbb{N}, p \in [2,3]$ |
| $I_{swh}$ | DW1000 transition current | 4 mA |
| $I_{sleep}$ | DW1000 sleep current | 1 $\mu$A |
| $t_{swh}$ | DW1000 transition time | 500 $\mu$s |
| $t_{ack}$ | DW1000 acknowledgement window | 50 ms |
| $BW$ | DW1000 bandwidth | 499.2 MHz |
| $I_{2,rx}$ | DW1000 mode 2 receive current | 244 mA |
| $I_{2,tx}$ | DW1000 mode 2 transmission current | 69 mA |
| $EPB_2$ | DW1000 mode 2 EPB | 44 nJ |
| $r_2$ | DW1000 mode 2 datarate | 6.8 Mbps |
| $PRF_2$ | DW1000 mode 2 pulse repetition frequencies | 16 |
| $Preamble_2$ | DW1000 mode 2 preamble size | 128 |
| $Code_2$ | DW1000 mode 2 preamble code | 3 |
| $CH_2$ | DW1000 mode 2 frequency | 3993.6 MHz |
| $I_{3,rx}$ | DW1000 mode 3 receive current | 191 mA |
| $I_{3,tx}$ | DW1000 mode 3 transmission current | 50 mA |
| $EPB_3$ | DW1000 mode 3 EPB | 2.1 $\mu$J |
| $r_3$ | DW1000 mode 3 datarate | 110 kbps |
| $PRF_3$ | DW1000 mode 3 pulse repetition frequencies | 64 |
| $Preamble_3$ | DW1000 mode 3 preamble size | 1024 |
| $Code_3$ | DW1000 mode 3 preamble code | 9 |
| $CH_3$ | DW1000 mode 3 frequency | 4492.8 MHz |

DEEPSLEEP, TX, RX, and SNOOZE. The average power consumption and detailed description for each of them is available in [23].

## V. REAL-TIME DISTANCE ESTIMATION AND DATA TRANSFER
### A. TWO-WAY RANGING
An asymmetric double-sided two-way ranging scheme (ATWR) [38] is used by Decawave SDK to calculate the distance between two DW1000 [39]. Using electronic and mathematical techniques to implement a clock with ps precision, the DW1000 can determine radio packet time of flight (TOF). Assuming the speed of radio waves as the same as the speed of light $c$, it is possible to use Eq. 2 to calculate the distance between the drone and sensor nodes.

$$d = c \cdot TOF \qquad (2)$$

In support of certain application scenarios, this two-way ranging has the advantage that it can be used in stand-alone mode without requiring complex infrastructure or fixed anchors [39]. ATWR is denoted asymmetric because it needs two transmissions and one reception, and does not require equal reply times from each device. It is composed of three messages: Poll, Response and Final. Using this method, the maximum error is in the low picosecond range, even
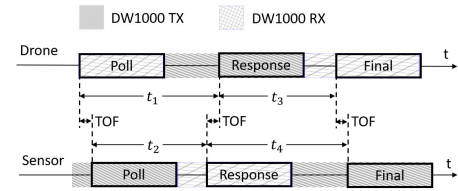


**FIGURE 4.** Asymmetric double-sided two-way ranging method. Sequences of packets for TOF estimation are shown.

with 20 ppm crystals, i.e. the worst-case specification [23]. This gives a theoretical error of approximately 2.2 mm. Each ATWR exchange consists of the drone sending the Poll message, receiving the Response message, and then transmitting the Final message. The protocol sequence and the TOF formula is in Fig. 4 and Eq. 3

$$TOF = \frac{t_1 t_4 - t_2 t_3}{t_1 + t_2 + t_3 + t_4}. \qquad (3)$$

Since $t_2$ and $t_3$ have a fixed and well known value, 800 $\mu$s with an error of $\pm 15.65$ ps, from $t_1$ and $t_4$ the MCU calculates the round trip time, which is two times the TOF. In this implementation of ATWR, the Response packet includes two fields: the previous TOF and the coil voltage. Having these values, the drone can calculate the distance using the previously calculated TOF and the coupling factor between coils, which is proportional to the measured voltage.

### B. ATWR RANGING PERFORMANCE
To design an accurate and reliable system, the ATWR was tested under both static and dynamic conditions. The static test was designed to measure the distance calculation accuracy and minimum working range of the UWB. Maximum coverage depends on the environment, multi-path fading and the DW1000 settings. On the other hand, the minimum range depends on clock drift and resolution, which impacts the TOF estimation [23]. Fig. 5 shows the results of 21 different tests in $Mode(2)$ and $Mode(3)$ (Table 2) at seven fixed distances: 10 cm, 20 cm, 90 cm, 3 m, and 5 m. The average measured distance and the standard deviation are a statistical result
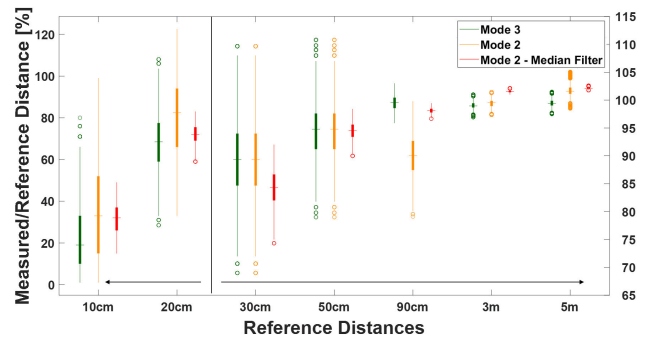


**FIGURE 5.** ATWR ranging performance in fixed positions. The graph shows the measurement variance of each test and the ratio between the reference and measured distance. The left part of the graph refers to the left scale, but the remaining refers to the right scale.

of over 75,000 points collected in a controlled environment. The error is the ratio between the reference and measured distances as a percentage, where the central mark indicates the median, and the bottom and top edges of the boxes indicate the $25^{th}$ and $75^{th}$ percentiles. The whiskers extend to the most extreme data points not considered outliers, which are plotted using the *o* symbol. As shown in Fig. 5, the 10 cm and 20 cm tests show that at such close range UWB is not reliable. Indeed, the Measured/Reference ratio in *Mode*(2) and *Mode*(3) is between 20% and 80%; and, the measurement span reaches up to 100%. The 30 cm test shows the threshold at which UWB becomes reliable. Although the variance is still high, the distance bias is 11%, corresponding to an error of 33 mm. In the 50 cm to 5 m tests, UWB performance improves significantly, with an average bias and variance below 5% and 20%, respectively, at 50 cm. Concerning the design of an accurate UAV landing/hovering algorithm, and taking into consideration the reported results in static conditions, the UWB's TOF data should only be used above 30 cm standoff between the drone and sensor board. Below this limit, using the coupling factor measurement is more accurate.

In addition to static analyses, twenty in-field evaluations were performed with a maximum speed of 60 km/h. Studying 100,000 collected data points, the UWB behaviour at varying speeds compared with the results in Fig. 5 was examined. Non-negligible packet loss due to fading and environmental noise was observed. With an average of 21% and a maximum of 80%, the experienced data loss can cause abrupt changes and vertical edges/spikes in the TOF estimation, which can cause unpredictable behaviour within a UAV landing algorithm. To avoid these issues, on top of our ATWR protocol a non-linear digital filter technique, the 1D-median-filter, was applied. As shown in Fig. 5, the median-filter with 21 entries (N) reduces the variance, averaging 3 times less. Despite improvements, this filter adds a time delay of $[int(N/2) + 1]$ that must be considered on the drone side to avoid errors during the execution of position estimation algorithm. Moreover, it was noticed that the median-filter biases the 30 cm test, adding an error of 5%. Over short distances, however, the algorithm uses both TOF and coupling factor $k$ to improve landing accuracy. On the other hand, the median-filter still decreases variance and noise with distances > 50 cm.

### C. ATWR RANGING PROTOCOL AND DATA TRANSFER

In the proposed framework, the drone and the sensor node operate as a pair. The drone operates as a ''Tag'' [23], initiating ranging, and the other acts as an ''Anchor'' [23], listening for the Tag's message. In addition to the ATWR packets (Fig. 4), the proposed UWB protocol presented in this work needs two other command messages, Blink and StartUp. Initially, the drone is in a discovery phase. It periodically sends a Blink message aiming to wake up the sensor node from the low power listening mode, and successively it listens for a response. If it is missed, the tag sleeps for a period (default

of 33 ms) before blinking again. The sensor node initially listens for the starting packet (Blink), and when the sensor node successfully receives a Blink message, it exits from the low power state, a duty cycled listen procedure in which the DW1000 periodically opens short receiver windows, entering to the ATWR ranging phase. When the UAV lands or hovers, the ATWR becomes unnecessary and the application can start to upload data from the sensor node. Then, the UAV sends the StartUP command to the STM32, which streams all the stored information to the UAV internal memory, *storage* in Fig. 1.

In our deployment, ATWR is performed in *Mode*(3) (see Table 2) to improve the maximum coverage up to 100 m, whereas the data transfer needs to be as fast as possible, thus the DW1000 is configured to *Mode*(2) featuring a baudrate $r_2$ of 6.8 Mbps. Payload throughput was extensively evaluated during in-field experiments, where the average payload throughput of 5.988 Mbps was achieved for a packet size of 1 kB and *Mode*(2). In the worst case, to upload the entire contents of the flash memory (256 MB), the time taken was 43 s. In this case, packet loss is negligible as the drone is stationary and the distance between devices is only a few centimetres.

## VI. ENERGY MODEL

To assist scheduling of drones for data collection and power transfer, energy consumption and data accumulation profiles for the sensor node must be modelled. Given different application scenarios, the sensors used coupled with their working principles result in wide variation in average energy consumption. Sensors with high sampling frequencies draw more power and result in intensive data generation. On the contrary, aggressively duty-cycled sensors consume negligible energy compared with other sensor node components, such as temperature and humidity that are commonly sampled at sub-Hz frequency. This contributes to the complexity of the sensor node's working pattern modelling. This section proposes a hierarchical method, which considers both perspectives of energy and data. Data collection and wireless power transfer could be scheduled accordingly. The sensor node energy model comprises three subsections. CPU energy modelling deals with the system CPU's energy consumption. RF energy modelling deals with energy consumption only happens within the RF core, such as transmitting and receiving a packet. Sensors modelling considers the energy profile of all sensors on board.

### A. SYSTEM CPU ENERGY MODELLING

The system CPU has three working modes; active mode, idle mode and standby mode. The active mode consumes the most energy, where all functionalities are enabled, while the stop mode consumes the least, but no operation is allowed. Current drawn is denoted $I_m^{MCU}$, shown in Table 2, where $m$ represents a mode $m \in \{active, idle, stop\}$. Apart from working current, current drawn during transition between modes is denoted $I_t^{MCU}$. The energy consumed during system MCU operation

can thus be written:

$$E_{MCU} = \sum_m V_s I_m^{MCU} T_m^{MCU} + \sum_t V_s I_t^{MCU} t_t^{MCU} N_t^{MCU}$$
$$+ V_s I_{BLE}^{MCU} T_{BLE}^{MCU} . \tag{4}$$

where $T_m^{MCU}$ is the sum of operation time of a mode. The fixed transition time between modes is denoted by $t_t^{MCU}$. $N_t^{MCU}$ is the number of transitions carried out during a period. $V_s$ is the supply voltage. $I_{BLE}$ and $T_{BLE}^{MCU}$ take into account the BLE transceiver and its dedicated ARM Cortex-M0.

### B. UWB SUBSYSTEM ENERGY MODELLING

A probabilistic approach to modelling a device's incoming and outgoing information flow can be shifted to a deterministic effort. It can be expected that the radio channel is silent for a long time, becoming busy only on UAV arrival and synchronisation. The UWB RF transceiver then shifts its modes between active and sleep. Transmitting and receiving currents are denoted $I_{p,tx}$ and $I_{p,rx}$ respectively, where the subscript $p$ indicates the protocol determined power. The transition current from $tx$ to $rx$, or $rx$ to $tx$ is defined as $I_{swh}$.

It is assumed the data volume to be sent to the UAV for a specific sensor is $PAY_{tot}$ in bytes, where $PAY_{max}$ is the maximum number of bytes per transmission. Given a data rate $r_p$, where $p$ represents a specific $Mode(p)$'s data rate, such as $r_2$ in Table 2, the time consumed for transmission is simply the division of the two. The acknowledgement time $t^{ack}$, ranging beaconing time $t_p^{rang}$, and $tx$-$rx$ switching time $t^{swh}$ is configuration dependent (cf. subscript $p$). It is assumed $N^{ack}$ acknowledgements are received during data transmission only if $A_s$ is equal to 1, otherwise null. The RF transmission energy consumption can then be modelled as in Eq. 7, where $E_{Ranging}$ in Eq. 5 and $E_{Data}$ in Eq. 6 are respectively the overall energy used for the two-way ranging protocol and the sensor node data transfer. In Eq. 5, a duty-cycled listen mode designed to reduce the average power consumption is considered, the DC variable spans between 1% to 7% for the application scenario, and $t^{DC}$ indicates the on time.

$$E_{Ranging} = V_s I_{p,rx} t_p^{rang} + V_s I_{p,rx} t^{DC} DC, \tag{5}$$

$$E_{Data} = 8 \cdot PAY_{tot} EPB_p + A_s ceil\left(\frac{PAY_{tot}}{PAY_{max}}\right)$$
$$\cdot \left(V_s I_{swh} t_p^{swh} + V_s I_{p,rx} t_{p,ack}\right), \tag{6}$$

$$E_{rf} = E_{Data} + E_{Ranging}, \tag{7}$$

$$t_p^{rang} = \frac{d'}{v} - \frac{\kappa}{d'} ln\left(\frac{0.01}{d'}\right). \tag{8}$$

Eq. 5 takes into consideration the ranging protocol settings for our deployment when the drone is approaching the sensor node. In Eq. 8 a ideal case scenario with exponential deceleration between $\kappa$ and the sensor node is modelled, considering hitting the first receive windows at $d'$ distance. $t_p^{rang}$ is defined as the time required for the drone to reach the sensor from the initial starting point.

### C. SENSORS ENERGY MODELLING

This section provides the energy consumption model of the internal sensors, expressed as energy per sample (EPS), a values that is independent of the acquisition frequency. Low frequency sensors, such as light, temperature, humidity, and pressure are considered as a single block, which needs 56 $\mu$J and 1.9 ms to collect the measured environmental conditions; Table 3. Inertial measurements are from LSM6DSOX and IIS2MDC, which need 7 ms and 265 $\mu$J to obtain 9-axis, see Table 3 for further details.

**TABLE 3.** Sensors energy modelling.

| ID | Sensor | Model | Max Op. Frequency | $T_{active}$ | EPS |
|---|---|---|---|---|---|
| a | Light | OPT3007 | 10 Hz | 1.9 ms | 56 $\mu$J |
| | Temperature | TMP117 | 1 Hz | | |
| | Humidity | HDC2080 | 1 Hz | | |
| | Pressure | BMP280 | 1 Hz | | |
| b | Accelerometer | LSM6DSOX | 9 kHz | 7.0 ms | 265 $\mu$J |
| | Magnetometer | IIS2MDC | 100 Hz | | |
| c | Microphone | IMP34DT05 | 2.4 MHz | cont | 26 mJ (16 ksps) |
| d | Microphone | MP23ABS1 | 20 kHz | cont | 99 $\mu$J (1 s) |
| e | Coil Voltage | STM32 - ADC | 10 kHz | cont | 1 $mJ$ (1 s) |

The audio sub-block energy consumption is given as EPS, defining one sample as one second of operation, yielding $\sim$16k samples. $DC_A$ is defined as the expected audio Duty Cycle, which is application dependent. It describes the percentage of operation in which the sound level is above the WUA threshold. Eq. 9 shows the sensor energy profile, excluding the external sensors that may be connected to the device and the WPT coil voltage (Table 3 - $e$). In Eq. 9, $N_s^x$ is the number of samples per application reference period.

$$E_{Sensors} = EPS^a N^a + EPS^b N^b$$
$$+ EPS^c DC_A + EPS^d (1 - DC_A). \tag{9}$$

Finally, the storage energy is modelled by the sum of the time required to erase a sector and the time required to write the data. The speed is assumed to be $b_a$, where $a \in \{read, write, erase\}$. Table 4 shows the equivalent EPB with a standard page-size (256 bytes). As expected, the erase power consumption heavily increases the average EPB, hence it is more convenient to clear the whole memory while the sensor node is powered by the mains or is under charging by the drone.

**TABLE 4.** Flash energy modelling.

| Device | Model | Operation | $b_a$ | EPB |
|---|---|---|---|---|
| Ext. Flash | MT25QL256ABA | $write + erase$ | 80 kB/s | 673 nJ |
| Ext. Flash | MT25QL256ABA | $write$ | 2 MB/s | 1.61 nJ |

### VII. EXPERIMENTAL RESULTS

Together with the full hardware project and the board driver source code, two application examples are provided [37]. To validate the energy model, battery lifetime estimation of

the APP1 [37] is presented, which consists of sampling and storing the internal sensor ID $a$ and $b$ (Table 3 and Table 4) at fixed frequency, 1 Hz and 12 Hz respectively. In this application, the sensor node expects to be recharged at programmed intervals, to restore the battery level and to collect the measured data. The DW1000's *DC* is 1%, and the drone approaching speed $v$ is programmed at 2 m/s. Uplink acknowledgements are disabled, hence $A_s$ is null. The STM32 does not apply any algorithm on the collected data, so it returns in *stop* mode between each sample. Lastly, the audio recording is turned off while the WUA is always active. $t_p^{rang}$, correspondent to ATWR time in Eq. 8, is equal to 26 s. Using these configurations, the average energy calculated by Eq. 10 is 79 J for one hour of operation, $t^{DC}$ equal to 3600 s, and one three stage landing procedure ($t_p^{rang}$). In one hour, sensor board collects more than 5 MB, using ($E_{MCU} + E_{Sensors}$) approximately 9.7 J, whereas the DW1000 in duty cycle mode needs 22.2 J.

$$E_{tot} = E_{MCU} + E_{rf} + E_{Sensors} \quad (10)$$

$$Days = \frac{E_{Battery}}{E_{tot}}. \quad (11)$$

With the proposed application settings, we estimate the battery lifetime using Eq. 11, which is approximately equal to one month.

We verified the proposed model assessing the sensor node behaviour in laboratory (static and controlled conditions) and in real environments. The measured average current consumption regarding the internal sensors acquisition is 0.84 mA, equivalent to 9.98 J, while the DW1000 needs 1.95 mA for 1% DC listening, which correspond to 23.2 J. Compared to our model, averaging on one hour of operation, these values differs by 3% and 4% respectively. These values are reflected in Fig. 6, where the logarithmic plot of the current profile shows all sensor node functionalities. Continuous sampling generates the 10 mA spikes, while the 190 mA spike comes from the DC listening of the DW1000. Finally, after a correct reception of a Blink message from the UAV, the ATWR is enabled, alternating transmission (lower current) and reception (higher current). Data transfer is not shown in Fig. 6, but is equal to a constant transmission current
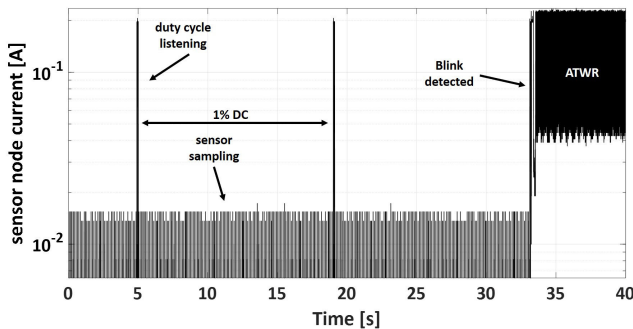
of *Mode*(3). An example of three stage landing is presented in Fig. 7, where the drone lands 38 s after the first Blink packet was received by the sensor node (point zero). Fig. 7 shows the same test from two points of view; on the left is plotted the planar route using the GPS and ATWR, which define the colorbar, while on the right distance estimation using both ATWR and WPT is presented. We acquired these values using the internal inertial module of the drone and its internal storage (Fig. 1). The test was performed with a strong lateral wind experienced in outdoor environment. Its speed reached up to 5 m/s. Fig. 8 shows the look-up table used by the drone to estimate the planar distance. It was obtained through a static estimation, and then assessed in our in-field experiments (Fig. 7). The table points to the measured coil voltage on the sensor node, which is considered to be indicative of the coupling factor. In this case, $E_{Ranging}$ becomes 24 J while the estimation is 45 J. In this case overestimating the landing energy cannot be considered as an error. Indeed, in a real
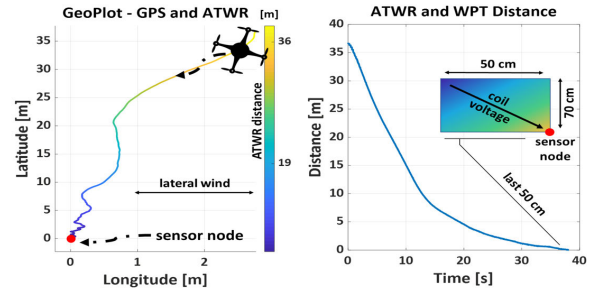


**FIGURE 7.** Experimental results from in-field tests of the hardware platform. Left: drone path in the presence of lateral wind, where ATWR defines the colorbar. Right: Estimated point-to-point distance using ATWR and WPT. Bottom: The drone correctly lands using the three stage method (not to scale).
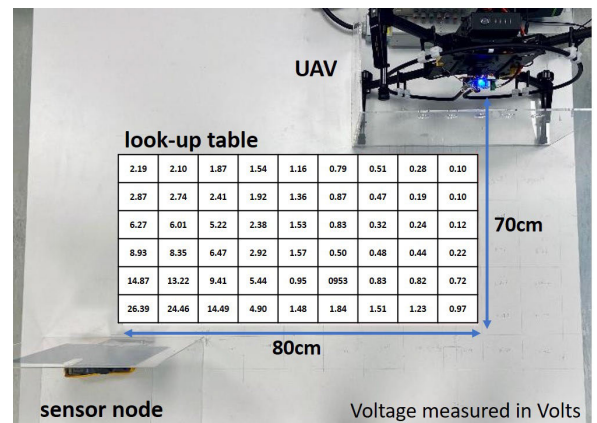


**FIGURE 6.** APP1 current profile during: sensor sampling, DC listening, and ATWR mode.



**FIGURE 8.** The look-up table is the result of an initial calibration, then used during the last landing stage.

environment, the UAV needs to change direction many times to correct for the effects of the lateral force of the wind. This effect is further increased during the final metres of the approach, where the speed is reduced and the propellers rotate more slowly, making it more difficult to combat the wind. Due to environmental wind instability is recommended to keep an energy buffer in the event that the drone would need more time to land correctly. Indeed, if the battery is completely discharged, the drone will be unable to land close to the IPT coil, since the UWB will be unreachable. Finally, during the last 50 cm that correspond to 4 s of flight, the WPT distance estimation compensates the ATWR error, allowing a landing precision of 25 cm even with strong lateral wind. A reliable estimation of the battery lifetime, in conjunction with the memory use, is a fundamental factor for the entire system. Indeed, the drone must visit each sensor within a maximum period given by Eq. 10 and Eq. 11.

## VIII. CONCLUSION

This article presented a low-power wireless sensor platform designed to integrate with UAVs with particular applicability in hazardous and extreme environments, where infrastructure communications may not exist and maintenance of devices is difficult for human operators. The platform features two localisation systems that exploit ATWR and coil coupling to improve position estimation to sub-metre precision, using a single reference point. The focus is on hardware design, with software developed for two application scenarios in addition to the three stage landing system. Modelling and in-field assessment of the platform's capabilities regarding battery lifetime are provided, showing that 30 days operation between charges is achievable for a sample application. It is shown that the energy model is valid around an error of 5%, supports adverse weather conditions and provides sufficient energy even where a drone needs to adjust landing path multiple times. This provides a framework in support of scheduling the UAV visits, which must occur before the energy buffer is depleted. As interoperability and flexibility are at the core of scientific research, the hardware design and supporting software for the platform are released as a fully open source project on GitHub [37].
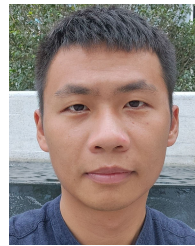
## ACKNOWLEDGMENT

## REFERENCES

[1] A. Kansal, J. Hsu, S. Zahedi, and M. B. Srivastava, "Power management in energy harvesting sensor networks," *ACM Trans. Embedded Comput. Syst. (TECS)*, vol. 6, no. 4, p. 32, 2007.

[2] P. D. Mitcheson, D. Boyle, G. Kkelis, D. Yates, J. A. Saenz, S. Aldhaher, and E. Yeatman, "Energy-autonomous sensing systems using drones," in *Proc. IEEE Sensors*, Oct. 2017, pp. 1–3.

[3] Y. Qin, D. Boyle, and E. Yeatman, "Radio diversity for heterogeneous communication with wireless sensors," in *Proc. IEEE 5th World Forum Internet Things (WF-IoT)*, Apr. 2019, pp. 955–960.

[4] Y. Qin, D. Boyle, and E. Yeatman, "Efficient and reliable aerial communication with wireless sensors," *IEEE Internet Things J.*, vol. 6, no. 5, pp. 9000–9011, Oct. 2019.

[5] H. P. Mistry and N. H. Mistry, "RSSI based localization scheme in wireless sensor networks: A survey," in *Proc. 5th Int. Conf. Adv. Comput. Commun. Technol.*, Feb. 2015, pp. 647–652.

[6] V. Djaja-Josko and J. Kolakowski, "Application of Kalman filter for positioning precision improvement in UWB localization system," in *Proc. 24th Telecommun. Forum (TELFOR)*, Nov. 2016, pp. 1–4.

[7] D. Palossi, F. Conti, and L. Benini, "An open source and open hardware deep learning-powered visual navigation engine for autonomous nano-UAVs," in *Proc. 15th Int. Conf. Distrib. Comput. Sensor Syst. (DCOSS)*, May 2019, pp. 604–611.

[8] J. N. Yasin, S. A. S. Mohamed, M.-H. Haghbayan, J. Heikko-nen, H. Tenhunen, and J. Plosila, "Unmanned aerial vehicles (UAVs): Collision avoidance systems and approaches," *IEEE Access*, vol. 8, pp. 105139–105155, 2020.

[9] M. Mueller, N. Smith, and B. Ghanem, "A benchmark and simulator for uav tracking," in *Proc. Eur. Conf. Comput. Vis.* Cham, Switzerland: Springer, 2016, pp. 445–461.

[10] A. Mittleider, B. Griffin, and C. Detweiler, "Experimental analysis of a uav-based wireless power transfer localization system," in *Experimental Robotics*. Cham, Switzerland: Springer, 2016, pp. 357–371.

[11] J. Kwak and Y. Sung, "Autonomous UAV flight control for GPS-based navigation," *IEEE Access*, vol. 6, pp. 37947–37955, 2018.

[12] J. M. Arteaga, L. Lan, S. Aldhaher, G. Kkelis, D. C. Yates, and P. D. Mitcheson, "A multi-MHz IPT-link developed for load characterisation at highly variable coupling factor," in *Proc. IEEE Wireless Power Transf. Conf. (WPTC)*, Jun. 2018, pp. 1–4.

[13] S. Aldhaher, P. D. Mitcheson, J. M. Arteaga, G. Kkelis, and D. C. Yates, "Light-weight wireless power transfer for mid-air charging of drones," in *Proc. 11th Eur. Conf. Antennas Propag. (EUCAP)*, Mar. 2017, pp. 336–340.

[14] M. Lu, M. Bagheri, A. P. James, and T. Phung, "Wireless charging techniques for UAVs: A review, reconceptualization, and extension," *IEEE Access*, vol. 6, pp. 29865–29884, 2018.

[15] C. Detweiler, M. Eiskamp, B. Griffin, J. Johnson, J. Leng, A. Mittleider, and E. Basha, "Unmanned aerial vehicle-based wireless charging of sensor networks," in *Wireless Power Transf. Algorithms, Technol. Appl. Ad Hoc Commun. Netw.*, pp. 433–464. Springer, 2016.

[16] B. Griffin and C. Detweiler, "Resonant wireless power transfer to ground sensors from a UAV," in *Proc. IEEE Int. Conf. Robot. Autom.*, May 2012, pp. 2660–2665.

[17] J. Tiemann, F. Schweikowski, and C. Wietfeld, "Design of an UWB indoor-positioning system for UAV navigation in GNSS-denied environments," in *Proc. Int. Conf. Indoor Positioning Indoor Navigat. (IPIN)*, Oct. 2015, pp. 1–7.

[18] G. Fantin, "UWB localization system for partially GPS-denied robotic applications," Ph.D. dissertation, Dept. Mechatronic Eng., Politecnico di Tori, Turin, Italy, 2019.

[19] R. Mocanu and A. Onea, "Indoor and outdoor vehicle localization using UWB transceivers," in *Proc. 27th Medit. Conf. Control Autom. (MED)*, Jul. 2019, pp. 299–303.

[20] A. Ledergerber, M. Hamer, and R. D'Andrea, "A robot self-localization system using one-way ultra-wideband communication," in *Proc. IEEE/RSJ Int. Conf. Intell. Robots Syst. (IROS)*, Sep. 2015, pp. 3131–3137.

[21] L. I. Balderas, A. Reyna, M. A. Panduro, C. Del Rio, and A. R. Gutierrez, "Low-profile conformal UWB antenna for UAV applications," *IEEE Access*, vol. 7, pp. 127486–127494, 2019.

[22] D. Dardari, P. Closas, and P. M. Djurić, "Indoor tracking: Theory, methods, and technologies," *IEEE Trans. Veh. Technol.*, vol. 64, no. 4, pp. 1263–1278, 2015.

[23] *Version DW1000 User Manual, 2.11.(Decawave, 2017)*, Dacawave, Dublin, Ireland, 2019.

[24] *15.4-2011 Uwb transceiver*, Standard DW1000 IEEE802 Datasheet, Decawave, 2016.

[25] J. Kulmer, S. Hinteregger, B. Grosswindhager, M. Rath, M. S. Bakr, E. Leitinger, and K. Witrisal, "Using DecaWave UWB transceivers for high-accuracy multipath-assisted indoor positioning," in *Proc. IEEE Int. Conf. Commun. Workshops (ICC Workshops)*, May 2017, pp. 1239–1245.

[26] A. Fotouhi, H. Qiang, M. Ding, M. Hassan, L. G. Giordano, A. Garcia-Rodriguez, and J. Yuan, "Survey on UAV cellular communications: Practical aspects, standardization advancements, regulation, and security challenges," *IEEE Commun. Surveys Tuts.*, vol. 21, no. 4, pp. 3417–3442, 4th Quart., 2019.

[27] H. Shakhatreh, A. H. Sawalmeh, A. Al-Fuqaha, Z. Dou, E. Almaita, I. Khalil, N. S. Othman, A. Khreishah, and M. Guizani, "Unmanned aerial vehicles (UAVs): A survey on civil applications and key research challenges," *IEEE Access*, vol. 7, pp. 48572–48634, 2019.

[28] G. Castellanos, M. Deruyck, L. Martens, and W. Joseph, "System assessment of WUSN using NB-IoT UAV-aided networks in potato crops," *IEEE Access*, vol. 8, pp. 56823–56836, 2020.

[29] G. Hattab and D. Cabric, "Energy-efficient massive IoT shared spectrum access over UAV-enabled cellular networks," *IEEE Trans. Commun.*, early access, May 29, 2020, doi: 10.1109/TCOMM.2020.2998547.

[30] H. Chao, Y. Cao, and Y. Chen, "Autopilots for small unmanned aerial vehicles: A survey," *Int. J. Control, Autom. Syst.*, vol. 8, no. 1, pp. 36–44, Feb. 2010.

[31] N. Hossein Motlagh, T. Taleb, and O. Arouk, "Low-altitude unmanned aerial vehicles-based Internet of Things services: Comprehensive survey and future perspectives," *IEEE Internet Things J.*, vol. 3, no. 6, pp. 899–922, Dec. 2016.

[32] J. Kelly, S. Saripalli, and G. S. Sukhatme, "Combined visual and inertial navigation for an unmanned aerial vehicle," in *Field and Service Robotics*. Berlin, Germany: Springer, 2008, pp. 255–264.

[33] J. L. Crassidis, F. L. Markley, and Y. Cheng, "Survey of nonlinear attitude estimation methods," *J. Guid., Control, Dyn.*, vol. 30, no. 1, pp. 12–28, Jan. 2007.

[34] A. Bahabry, X. Wan, H. Ghazzai, H. Menouar, G. Vesonder, and Y. Massoud, "Low-altitude navigation for multi-rotor drones in urban areas," *IEEE Access*, vol. 7, pp. 87716–87731, 2019.

[35] *Shenzhen Dajiang Baiwang Technology Co., Ltd*, DJI, Shenzhen, China, 2020.

[36] S. Liu, J. Su, and J. Lai, "Accurate expressions of mutual inductance and their calculation of archimedean spiral coils," *Energies*, vol. 12, no. 10, p. 2017, May 2019.

[37] (2020). *Open Source Repository*. [Online]. Available: https://github.com/tommasopolonelli/synthsense-wsn-uav

[38] *ASP013: The Implementation of Two-Way Ranging With the DW1000*, Decawave Limited, Dublin, Ireland, 2015.

[39] M. Malajner, P. Planinsic, and D. Gleich, "UWB ranging accuracy," in *Proc. Int. Conf. Syst., Signals Image Process. (IWSSIP)*, Sep. 2015, pp. 61–64.

**YUAN QIN** (Student Member, IEEE) received the bachelor's degree from The Hong Kong Polytechnic University, in 2014, and the master's and Ph.D. degrees in electronics engineering from Imperial College London, in 2015 and 2020, respectively. He is currently a Researcher with Huawei Technologies Company Ltd. His research interests include wireless communication protocols, autonomous unmanned vehicles, and power management techniques.

**ERIC M. YEATMAN** (Fellow, IEEE) received the B.Sc. degree from Dalhousie University, Canada, in 1983, and the Ph.D. degree from Imperial College London, in 1989. He is currently a Professor of micro-engineering and the Head of the Department of Electrical and Electronic Engineering, Imperial College London. His research interests include motion and thermal energy harvesting for wireless devices, pervasive sensing, and sensor networks. He is a Fellow and Silver Medalist of the Royal Academy of Engineering. He is the Co-Founder and the Director of Microsaic Systems that develops and markets miniature mass spectrometers for portable chemical analysis.

**LUCA BENINI** (Fellow, IEEE) received the Ph.D. degree from Stanford University, in 1997. He holds the Chair of digital circuits and systems with ETHZ. He is currently a Full Professor with the Università di Bologna. He has published more than 1000 peer-reviewed articles and five books. His research interests include energy-efficient parallel computing systems, smart sensing micro-systems, and machine learning hardware. He is a Fellow of the ACM and a member of the Academia Europea.

**TOMMASO POLONELLI** (Student Member, IEEE) received the bachelor's and master's degrees in electronics engineering from the University of Bologna, Bologna, Italy, in 2013 and 2017, respectively, where he is currently pursuing the Ph.D. degree. He is a Teaching Tutor with the University of Bologna. He has collaborated with several universities and research centers, such as the University College Cork, Cork, Ireland, Imperial College London, London, U.K., and the ETH, Zurich, Switzerland. He has authored over 15 articles in international journals and conferences. His research interests include wireless sensor networks, autonomous unmanned vehicles, power management techniques, and the design of batteries-operating devices and embedded video surveillance.

**DAVID BOYLE** (Member, IEEE) received the B.Eng. and Ph.D. degrees in computer and computer and electronic engineering from the University of Limerick, Limerick, Ireland, in 2005 and 2009, respectively. He is currently a Lecturer with the Dyson School of Design Engineering, Imperial College London. His research interests include security, privacy, and trustworthiness of connected monitoring and control systems.

• • •